Available online at www.sciencedirect.com
SCIENCE DIRECT®
Journal of Solid State Chemistry 178 (2005) 1539–1550
JOURNAL OF SOLID STATE CHEMISTRY
www.elsevier.com/locate/jssc

Lamellar and filament-like crystals of misfit-layer compounds containing (Sm, Ta, S) and (Pb, Bi, Nb, S) elements

Youichi Ohno*

Department of Electrical and Electronic Engineering, Faculty of Engineering, Utsunomiya University, 7-1-2 Yoto, Utsunomiya 321-8585, Tochigi, Japan

Received 24 November 2004; received in revised form 22 February 2005; accepted 27 February 2005
Available online 25 March 2005

Abstract

This paper presents the preparation and characterization of filament-like crystals as well as lamellar crystals for misfit-layer compounds containing (Sm, Ta, S) and (Pb, Bi, Nb, S) elements. They were grown by chemical-vapor transport reaction. The crystal structure and morphologies are investigated by transmission and reflection X-ray diffraction (XRD) and scanning electron microscopy (SEM). Filament-like crystals of $(SmS)_{1.19}TaS_2$ and $\{(Nb_{1-y-z}Pb_yBi_zS)_{1.5}\}_{1+x}NbS_2$ are grown abundantly. They belong to a large family of 1Q/1H and 1.5Q/1H types of misfit-layer compounds. They have an asymmetric layered structure, constructed of Q (SmS and $Nb_{1-y-z}Pb_yBi_zS$) and H (NbS_2) layers alternately stacked along the c axis. The lattice parameters of $\{(Nb_{1-y-z}Pb_yBi_zS)_{1.5}\}_{1+x}NbS_2$ are scarcely dependent on the amounts of Pb and Bi in raw materials, excluding a slight distortion in a crystal structure from the orthorhombic to the monoclinic. A comparison with the XRD results of the lamellar crystals of $(Pb_{1-y'}Bi_{y'}S)_{1+x'}(NbS_2)_n$ ($n = 1$ and 2) shows that Bi is in a higher oxidation state than Pb. However, both elements are contained only slightly in the filament-like crystals. The preliminary two-probe measurements of the temperature-dependent resistance have been made. The results indicate that there are two distinct types with positive and negative temperature coefficients.

Keywords: Misfit-layer compounds; Nanotubes; Microtubes; Filament-like crystals

1. Introduction

Various nanotubes (NTs) and microtubes (MTs) have been paid great attention since 1991 when carbon NTs were discovered by Iijima [1], because they exhibit many fascinating properties such as one-dimensional quantum effects and high flexibility and have various potential applications to hydrogen storage, solid-state secondary batteries, filtering media and nanoscale electronic devices [2]. Layered transition-metal dichalcogenide (LTMD) NTs were firstly discovered by Tenne el al. [3] in the next year. Since then, LTMD NTs and MTs have been studied extensively. Up to date they were grown for TiS_2 [4], $TiSe_2$ [5], ZrS_2 [6] and HfS_2 [6] (Group IV a compounds), NbS_2 [6,7], $NbSe_2$ [8] and TaS_2 [6,9] (Group V a compounds) and MoS_2 [10–12], WS_2 [3,12,13], $MoSe_2$ [14] and WSe_2 [14] (Group VI a compounds) by various methods including the annealing technique of oxidized transition-metal films in a H_2S flow, the hydrogen reduction or thermal decomposition of transition-metal trisulfides and iodine chemical transport reaction. It is found that there are many similarities in growth modes and morphologies between carbon and LTMD NTs. Recently, Nath et al. [8] have shown that $NbSe_2$ NTs are metallic, exhibiting superconductivity below 8.3 K. Chen et al. [15] and Dominko et al. [16] have indicated that MoS_2 NTs can store a relatively large amount of hydrogen in gaseous and electrochemical storage and exchange lithium in non-aqueous electrolytes. The maximum amount of inserted lithium was typically 2.3 per molecule for NT bundles. This value was larger than that of layered 2H-MoS_2.

*Corresponding author. Fax: +81 28 689 6009.
E-mail address: ohno@cc.utsunomiya-u.ac.jp.

0022-4596/$ - see front matter © 2005 Elsevier Inc. All rights reserved.
doi:10.1016/j.jssc.2005.02.021

The misfit-layer compounds, which are denoted by the chemical formula $\{(MX)m\}_{1+x}(TX_2)_n$ (M = Sn, Sb, Pb, Bi and rare-earth elements; T = Ti, V, Cr, Nb and Ta; X = S and Se; $x = 0.08$–0.28; $m = 1$, 3/2 and 2; $n = 1$, 2, 3 and 4), have a high potentiality to form tubular crystals as firstly been indicated by Guemas et al. [17], because they have an asymmetric layered structure constructed of two- or three-atom-thick MX layers and three-atom-thick TX_2 layers periodically stacked along the c-axis. They are regarded as the intercalation derivatives of LTMDs in a broad sense. A TX_2 layer is identical to a slab in LTMDs and the energy band structure is not significantly affected by the insertion of a MX layer except for the up-shift of the Fermi level. Atomic species in a TX_2 layer are arranged in pseudo-hexagonal geometry, so that it is customarily called a H layer. As a MX layer has pseudo-quadratic symmetry, then it is called a Q layer. For lamellar crystals they are incommensurate along the a-axis. The incommensurability parameter, which is defined by $\alpha = a_H/a_Q$, where a_H and a_Q are the lattice parameters in the a directions of the H and Q layers, respectively, is then irrational. Fig. 1 shows the schematic diagrams of ideal single-walled NTs for the 1Q/1H and 1.5Q/1H types of compounds. 1Q/1H compounds consist of three-atom-thick H layers and two-atom-thick Q layers alternately stacked while 1.5Q/1H compounds consist of three-atom-thick H layers and three-atom-thick Q layers alternately stacked. An asymmetric layered structure has a tendency to curl up a thin crystalline sheet, because a stress acts on either side of individual layers in a different manner. However, the MT or NT growth has been reported only for $(PbS)_{1.14}(NbS_2)_n$ [18] and $(BiS)_{1+x}(NbS_2)_n$ ($n = 1$ and 2) [19] till now. We may expect that the tubular crystals containing a rare-earth metal reveal interesting magnetic properties if they are synthesized.

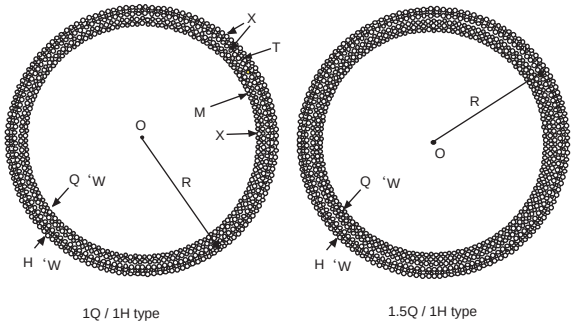

Fig. 1. Schematic diagram for the single-walled nanotubes of the 1Q/1H and 1.5/1H types of misfit-layer compounds. The single-walled NTs of the 1Q/1H type consist of a three-atom-thick H layer and a two-atom-thick Q layer while those of the 1.5Q/1H type consist of a three-atom-thick H layer and a three-atom-thick Q layer. T is a transition-metal, M is a metal atom including Pb, Bi and Sm, and X is a chalcogen atom. Outer radius (R) is about 7 nm.

This paper presents the preparation and characterization of filament-like crystals for misfit-layer compounds containing (Pb, Bi, Nb, S) and (Sm, Ta, S) elements as well as lamellar crystals. Filament-like crystals which are grown abundantly are identified to be the MTs and NTs of $\{(Nb_{1-y-z}Pb_yBi_zS)_{1.5}\}_{1+x}NbS_2$ and $(SmS)_{1.19}TaS_2$ whereas lamellar crystals and thick-walled multilayer cylindrical tubes of diameters extending 100 μm are $(Pb_{1-y'}Bi_{y'}S)_{1+x'}(NbS_2)_n$ ($n = 1$ and 2) and $(SmS)_{1.19}TaS_2$. The morphologies of the filament-like crystals are investigated by means of the scanning electron microscopy (SEM) method. The crystal structure is discussed in the light of known results.

2. Experiments

The filament-like crystals of $\{(Nb_{1-y-z}Pb_yBi_zS)_{1.5}\}_{1+x}NbS_2$ and $(SmS)_{1.19}TaS_2$ and the lamellar crystals of $(Pb_{1-y'}Bi_{y'}S)_{1+x'}(NbS_2)_n$ ($y' = 0$, 0.18, 0.33 and 1; $n = 1$ and 2) and $(SmS)_{1.19}TaS_2$ were obtained by chemical vapor transport reaction in attempt to synthesize the thinner tubular crystals of diameters less than 1 μm or the NTs of $(Pb_{1-y'}Bi_{y'}S)_{1+x'}(NbS_2)_2$ ($y' = 0$, 0.18, 0.33 and 1) and $(SmS)_{1.19}(TaS_2)_2$. The mixture of stoichiometric amounts of elements was placed in an evacuated and then closed silica tube of inner-diameter of 15 mm and length of about 300 mm. In the (Pb, Bi, Nb, S) system a small amount of $PbCl_2$ or $BiCl_3$ was added to raw materials to generate Cl_2 gas employed as a transport reagent. The silica tube was placed in a two-zone electric furnace. It was heated to 600 °C gradually to avoid explosion. Afterwards the high- and low-temperature zones of a furnace were kept at 650 and 600 °C for a week and 900 and 850°C for 2 weeks. In the (Sm, Ta, S) system the stoichiometric powder of Sm_2S_3, Ta, and S was placed in a closed silica tube with a small amount of iodine employed as a transport reagent and then was heated to 900 °C gradually. Afterwards the high and low temperature zones of a furnace were kept at 960 and 910 °C for 3 weeks. The filament-like crystals of $\{(Nb_{1-y-z}Pb_yBi_zS)_{1.5}\}_{1+x}NbS_2$ and $(SmS)_{1.19}TaS_2$ were grown in the lower-temperature region than the lamellar crystals of $(Pb_{1-y'}Bi_{y'}S)_{1+x'}$ $(NbS_2)_n$ and $(SmS)_{1.19}TaS_2$, respectively.

Grown crystals were analyzed by means of transmission and reflection X-ray diffraction (XRD) methods. The former brings the structural information of the (a, b) plane of a lamellar crystal whereas the latter does the information along the c-axis. A specimen holder in a Rigaku X-ray diffractometer was improved to allow transmission measurements. Our X-ray diffractometer in the transmission mode is illustrated schematically in Fig. 2. A goniometer was set at a given Bragg angle (θ) and a sample was rotated about a normal to a specimen

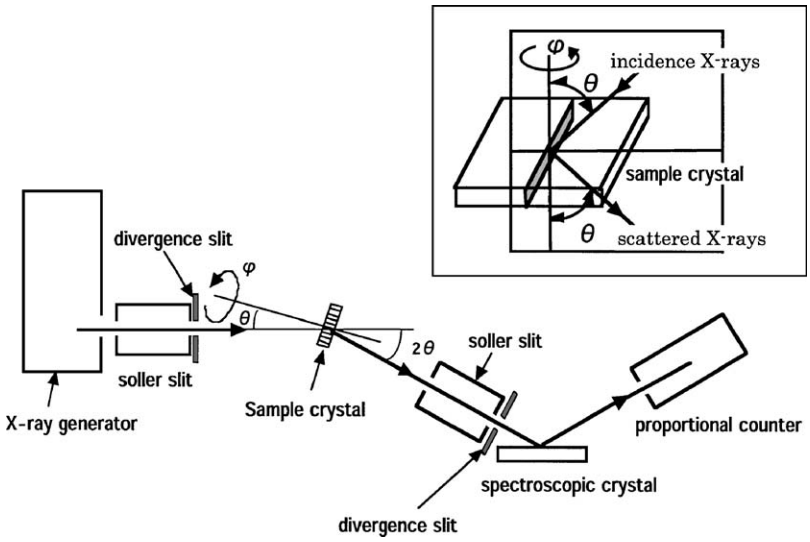

Fig. 2. Schematic diagram for our X-ray diffractometer in the transmission mode. An inset shows the rotation of a sample crystal against X-rays.

plane (ø rotation). The θ angle was then changed by 0.1° and the ø rotation was repeated. These measurements were performed in the 2θ range of 28–33° repeatedly. Cu $K\alpha$ X-rays (wavelength of 1.54056 Å) are used. They are emitted from an X-ray tube and then are passed through a soller slit and a divergence slit to result in a parallel incident beam. Thin-film samples for transmission measurements were prepared by cleaving a lamellar crystal with adhesive tape. The XRD samples of filament-like crystals were prepared by sprinkling a lot of crystals on adhesive tape on a glass holder. Their XRD patterns were measured in the reflection mode, in which X-rays were reflected intensively with crystal planes parallel to layers when satisfying the Bragg condition.

A scanning electron microscope equipped with an energy-dispersive analyzer was used to investigate morphologies and chemical compositions. SEM observations were done at beam voltage of 20 kV. The clean surfaces of lamellar crystals were prepared by a cleavage just before the measurements, although no surface cleaning was done for filament-like crystals. Scanning tunneling microscope (STM) images were obtained in the constant current mode in ultra-high vacuum. It is known that NTs prepared by chemical transport reaction are covered with an amorphous-like material of inhomogeneous thickness [20]. Then filament-like crystals were heated at about 300 °C in vacuum for a few hours before STM observations. Their images were taken at tunneling current of 0.6 nA and bias voltage of 0.55 V, using a mechanically polished Pt–Ir tip.

Temperature-dependent electrical resistance was measured for the filament-like crystals of $\{(Nb_{1-y}Pb_yS)_{1.5}\}_{1+x}NbS_2$ by the two-probe method. The measurements were done automatically, using a multimeter and electrical sources which were controlled by a personal computer. Electrical contacts were made with 0.05 mm diameter gold wires and conductive silver paste. Temperature measurements were done with a *K* (alumel–chromel) thermocouple.

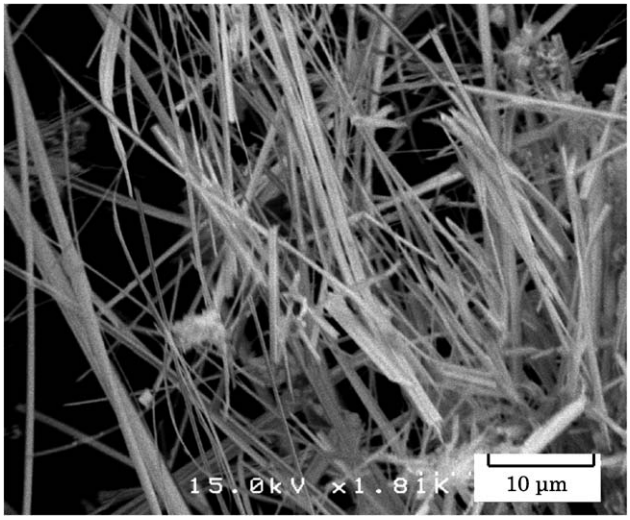

Fig. 3. SEM image of the NTs or MTs of $(SmS)_{1.19}TaS_2$.

3. Results and discussion

3.1. Filament-like crystals in the (Sm, Ta, S) system

The filament-like crystals of $(SmS)_{1.19}TaS_2$ are grown abundantly by iodine chemical-vapor transport reaction. They are black and quite lengthy, some being more than a millimeter long as shown in Fig. 3. They have excellent mechanical properties. They are easily bent, but are restored when removing an applied stress

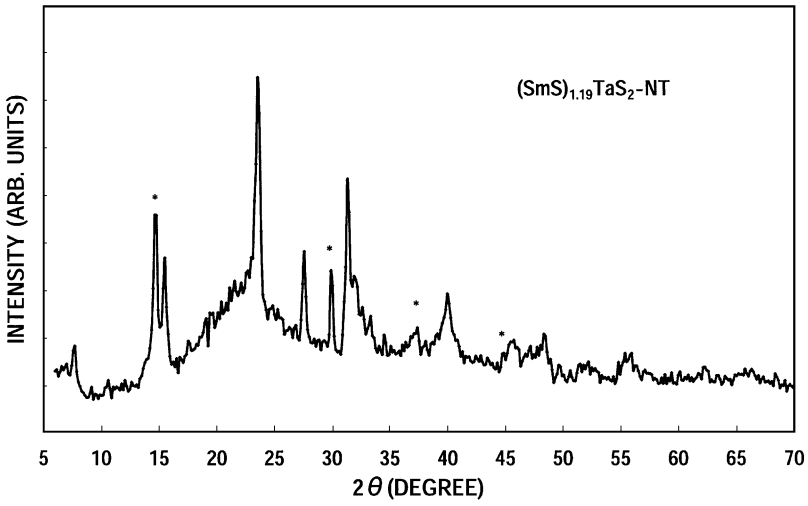

Fig. 4. XRD pattern of the NTs or MTs of $(SmS)_{1.19}TaS_2$. Diffraction lines with an asterisk mark are attributed to TaS_2 crystals.

because of high elasticity. The XRD pattern is shown in Fig. 4. It is found that TaS_2 is mixed in the form of a filament crystal or contained as a composite crystal. The term 'composite crystal' used here means that a crystal is made up of more than two different kinds of crystal parts. The composite crystals are often found in the crystal growth of multinary-layered compounds and intergrowth compounds. In most cases they are accompanied with crystal imperfections such as a stacking fault. A typical XRD pattern reveals more than two sets of diffraction lines as shown in Fig. 4. Unfortunately, no XRD measurements were carried out for individual crystals owing to technical difficulties. Measured XRD data for the crystal part of $(SmS)_{1.19}TaS_2$ are compared with calculated results in Table 1. Lattice parameters used for calculation are obtained from lamellar crystals, which agree with those of Wiegers et al. [21]. The diffraction lines of types a and b are derived from the sub-lattices of SmS and TaS_2 layers, respectively, while the diffraction lines of type c are common for both the sub-lattices. It is found that there is an agreement between measured and calculated values.

In a TaS_2 crystal part in a mixture or a composite crystal the layer thickness is 6.01 Å. This value is larger by 0.11 and 0.04 Å than those of 1T- and 3R-TaS_2, respectively, although it is smaller by 0.02 Å than that of 2H-TaS_2. According to Nath and Rao [6], the unit cell expands by 3% along the c-axis for the NTs of diameters less than 100 nm. Our crystals are mostly larger in diameter than those of Nath and Rao. Then we may consider that lattice strains are too small to result in lattice expansion. Recently, Remškar et al. [12] have indicated that MoS_2 and WS_2 NTs which are produced by chemical vapor transport, are the 2H-polytype, although the MTs of diameters extending 1 μm and lengths of few hundreds of micrometers prefer the 3R-polytype. If their result is applied to TaS_2 as well, the 3R-polytype would be most probable. If so, the unit cell expands by about 0.7%.

Table 1
X-ray diffraction pattern for the filament-like crystals of $(SmS)_{1.19}TaS_2$

hkl	Type	$2\theta_{obs}$	$2\theta_{calc}$
0 0 2	*c*	7.73	7.83
0 0 4	*c*	15.50	15.74
0 1 2	*c*	17.66	17.48
1 0 2	*a*		17.80
0 0 6	*c*	23.57	23.71
1 0 1	*b*	27.55	27.37
1 1 4	*a*		27.48
1 1 0	*b*		31.39
0 2 0	*c*	31.40	31.47
1 1 1	*b*		31.63
0 0 8	*c*		31.79
2 0 0	*a*	32.06	32.22
2 0 1	*a*	32.64	32.47
0 2 2	*c*		32.49
2 0 2	*a*	33.36	33.21
1 1 3	*b*		33.64
2 0 3	*a*	34.51	34.42
0 0 10	*c*	39.98	40.04
2 2 0	*a*	45.74	45.67
2 0 8	*a*		45.89
0 0 12	*c*	48.48	48.51
2 0 0	*b*		55.84
2 0 1	*b*	55.97	56.00
1 3 1	*b*		56.15
0 0 14	*c*	57.12	57.28
11 14	*a*	62.30	62.27
22 10	*a*		62.32
0 0 16	*c*	66.48	66.43

Type a: SmS part ($a = 5.55, b = 5.68$ and $c = 2250$ Å). Type b: TaS_2 part ($a = 3.29, b = 5.68$ and $c = 2250$ Å). Type c: common.

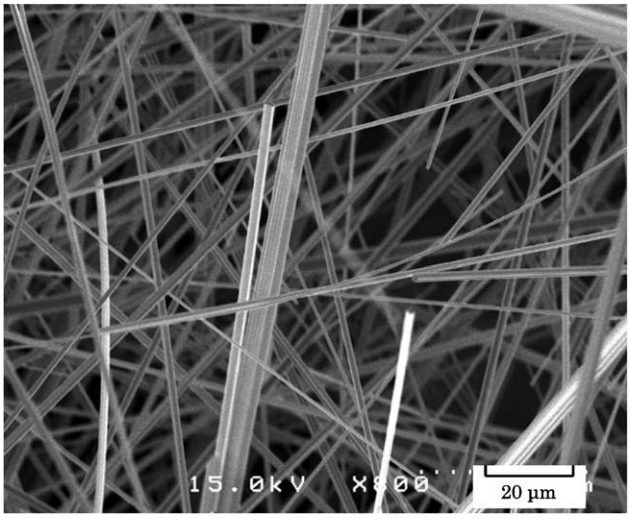

Fig. 5. SEM image of the NTs or MTs of $(Nb_{1-z}Bi_zS)_{1+x}NbS_2$.

3.2. Filament-like crystals in the (Pb, Bi, Nb, S) system

Fig. 5 shows the filament crystals of $\{(Nb_{1-z}Bi_zS)_{1.5}\}_{1+x}NbS_2$ which belongs to the 1.5Q/1H type of misfit-layer compounds. They are often grown from the indented or the waved edges of lamellar crystals together with ribbon-like crystals. A SEM image in Fig. 6(a) shows the ribbon-like crystals of $\{(Nb_{1-z}Bi_zS)_{1.5}\}_{1+x}NbS_2$, which are generated from a thin plate at the edge of the lamellar crystal of $(BiS)_{1.08}NbS_2$. The ribbon-like crystals grow in a direction parallel to the commensurate b direction of a lamellar crystal preferentially. In a few cases with a stacking fault as discussed below they grow in a direction rotated by 30° around a normal to layers. Some ribbon-like crystals begin to roll up perpendicularly to a growth direction to minimize a lattice strain and form a tubular crystal (see Fig. 6(b)). The thinner the sheet consisting of asymmetric layers, the larger the deformation due to a bending moment giving rise to spontaneous bending [18]. A similar situation has been found in the initial growth of MoS_2 MTs although the folding of a weakly bonded crystalline sheet results from the instability of growth conditions [22].

Fig. 7 shows the SEM images of various apexes or cross sections. A thin-walled cylindrical tube in Fig. 7(a) and a heavily deformed tube in Fig. 7(b) are vacant inside a wall. The wall thickness of a cylindrical tube is about 10 nm, which corresponds to seven pairs of layers. As it is observed carefully, we can find small crystals of a diameter less than 10 nm on the wall, which are smallest among the filament-like crystals observed in this study. A tube in Fig. 7(b) has a faceted wall. Each narrow strip on the wall consists of a planar crystal elongating along a tube axis. Because the misfit-layer compounds are easily cleaved into many strips, the faceted wall is

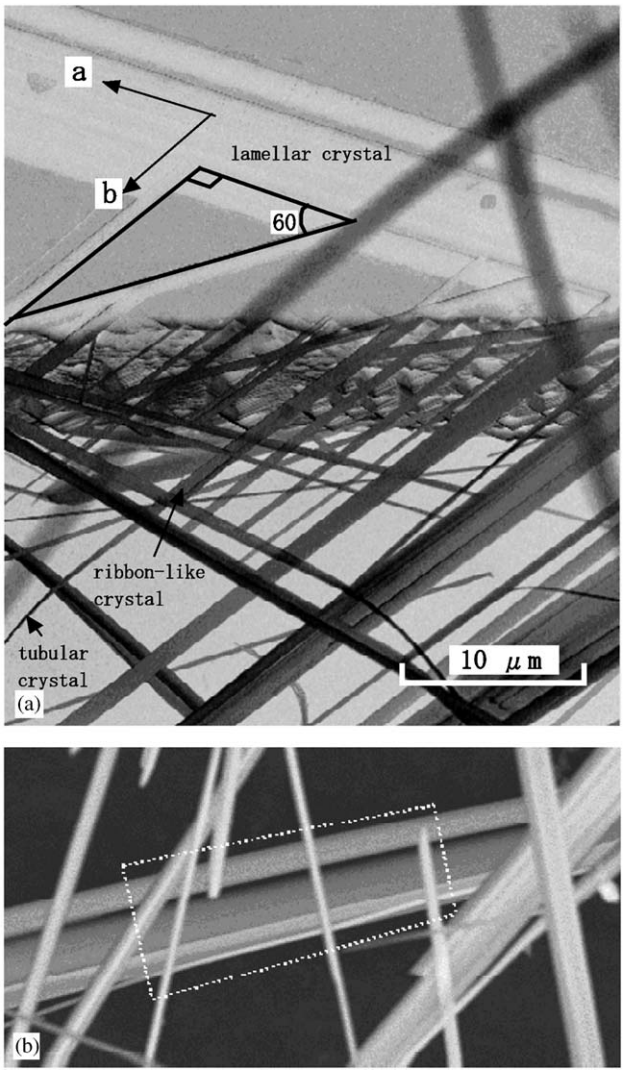

Fig. 6. (a) SEM image of the ribbon-like crystals of $\{(Nb_{1-z}Bi_zS)_{1.5}\}_{1+x}NbS_2$, which are generated from the intended edge of the lamellar crystal of $(BiS)_{1.08}NbS_2$. (b) Some of them begin to bend and roll up in the shape of a tube.

considered to be produced by a lattice strain of an asymmetric layered structure. Fig. 7(c) shows a filament-like crystal with a gear-like cross section. Its crystal is filled completely inside a wall and convex portions outside a wall are constructed of layers expanding in a radial direction. Such a structure may be formed by layer-growth from the vapor phase after the completion of a tube. A SEM image in Fig. 7(d) shows small steps near a tapered end, which gives the evidence of rolling up a crystalline sheet. A SEM image in Fig. 7(e) shows deposited particles which can behave as catalyst particles. A NT in Fig. 7(f) is terminated by a crater with small cones at a center and a periphery. A similar NT has been found for WS_2, in which a small-truncated cone in the center has a hole of inner diameter less than 2 nm [12].

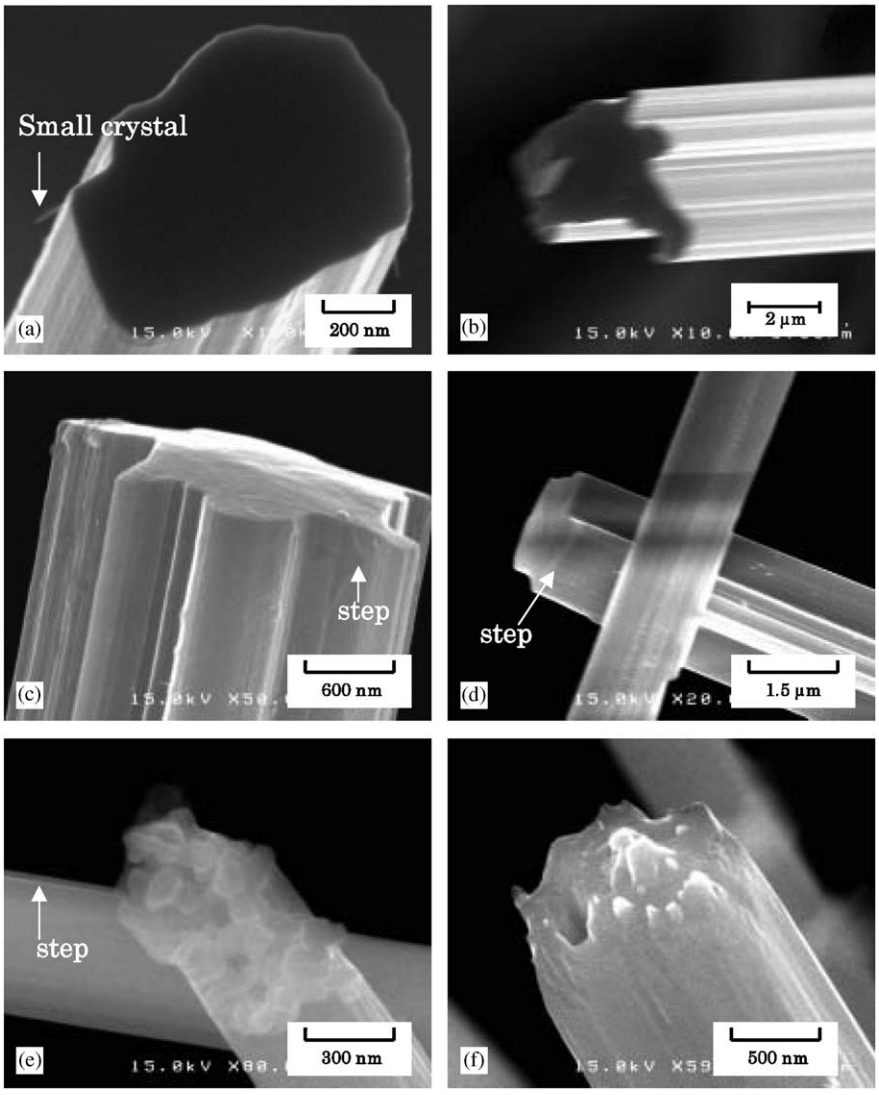

Fig. 7. SEM images of the various apexes or cross sections of the filament crystals of $(Nb_{1-z}Bi_zS)_{1+x}NbS_2$ ((a)–(d)) and $(Nb_{1-y}Pb_yS)_{1+x}NbS_2$ ((e)–(f)). (a) A distorted cylindrical tube with a thin wall. Small filament crystals of radii less than 10 nm are grown from the wall. (b) A deformed tube with a faceted wall. Many strips are observed in the axial direction. (c) A filament-like crystal with a closed apex and a gear-like cross section. Convex portions outside of a wall enlarge by layer growth. (d) Two crossed crystals with a taper end. A step appears near the end. (e) A filament crystal terminated by deposited particles. (f) NT bundle terminated by a crater with small cones at a center and a periphery.

Fig. 8 shows the XRD patterns of the filament-like crystals grown in the same silica ampoule as the lamellar crystals of $(BiS)_{1.08}NbS_2$, $(Pb_{0.82}Bi_{0.18}S)_{1.14}NbS_2$, $(Pb_{2/3}Bi_{1/3}S)_{1.14}NbS_2$ or $(PbS)_{1.14}NbS_2$. Most of the filament-like crystals are $\{(Nb_{1-y-z}Pb_yBi_zS)_{1.5}\}_{1+x}NbS_2$ although a small number of $(Pb_{1-y'}Bi_{y'}S)_{1+x'}NbS_2$ NTs and MTs grow at the same time. The 2θ positions of the intensive lines, which are attributed to the filament-like crystals of $\{(Nb_{1-y-z}Pb_yBi_zS)_{1.5}\}_{1+x}$ NbS_2, are scarcely dependent on the Bi quantity of raw materials although some lines are split into two or three peaks by reduced symmetry in a crystal structure. Bi-free crystals have an orthorhombic unit cell. Measured 2θ values of $\{(Nb_{1-y}Pb_yS)_{1.5}\}_{1+x}NbS_2$ and $\{(Nb_{1-z}Bi_zS)_{1.5}\}_{1+x}NbS_2$ are compared with calculated ones in Tables 2 and 3, respectively. As a Bi content increases, the unit cell is distorted into the monoclinic structure. Weak diffraction lines, which are marked by an asterisk are, on the other hand, shifted to lower angle with a Pb content. Their 2θ values agree with those of the (00ℓ) lines of $(Pb_{1-y'}Bi_{y'}S)_{1+x'}NbS_2$ which are measured for lamellar crystals and discussed later. Lattice parameters, polytypes and incommensurability parameters (α) obtained are tabulated in Table 4 together with those of related misfit-layer compounds. The a_H value for $\{(Nb_{1-y-z}Pb_yBi_zS)_{1.5}\}_{1+x}NbS_2$ is estimated from the b lattice parameter, using the relation $a_H = b/\sqrt{3}$. Except for $(BiS)_{1.08}NbS_2$ the α values are close to 4/7. If α is rational, $Nb_{1-y-z}Pb_yBi_zS$ and NbS_2 layers are commensurate, resulting in a superlattice with

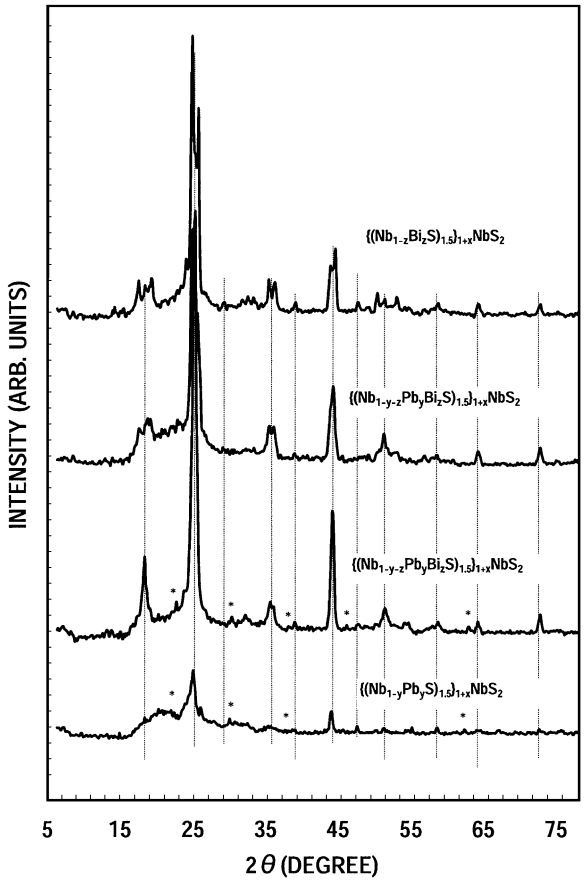

Fig. 8. XRD patterns of the NTs or MTs of $\{(Nb_{1-y-z}Pb_yBi_zS)_{1.5}\}_{1+x}NbS_2$, which are obtained from the same silica ampoule as the lamellar crystals of $(BiS)_{1.08}NbS_2$, $(Pb_{0.82}Bi_{0.18}S)_{1.14}NbS_2$, $(Pb_{2/3}Bi_{1/3}S)_{1.14}NbS_2$ or $(PbS)_{1.14}NbS_2$. The amount of Bi in raw materials increases while going from the bottom to the top. Small diffraction lines with an asterisk mark are attributed to the filament-like crystals of $(Pb_{1-y'}\ Bi_{y'}S)_{1+x'}NbS_2$.

Table 2
X-ray diffraction pattern for the filament-like crystals of $\{(Nb_{1-y}Pb_yS)_{15}\}_{1+x}NbS_2$. $a = 23.2, b = 5.80, c = 14.23$ Å

hkl	$2\theta_{obs}$	$2\theta_{calc}$
4 0 0	14.93	15.26
0 1 0		15.26
2 1 1	18.38	18.19
0 0 3		18.69
0 1 3	24.14	24.21
0 0 4	25.01	25.01
4 1 2		25.04
7 1 0	31.20	31.05
0 0 5		31.41
4 1 4	33.50	33.31
7 1 2		33.57
2 1 5	35.70	35.95
6 0 5	39.10	39.27
4 2 3		39.57
4 1 6		44.07
0 0 7	44.16	44.53
0 2 5		44.57
4 0 7	47.62	47.36
12 0 1		47.42
0 0 8		51.32
8 2 4	51.22	51.39
12 1 2		51.40
8 2 5	55.10	55.16
0 0 9	58.56	58.31
1 0 9		58.46
16 0 0		64.18
0 4 0	64.32	64.18
8 2 7		64.49
0 4 1		64.55
00 11	72.87	73.09

Table 3
X-ray diffraction pattern for the filament-like crystal of $\{(Nb_{1-z}Bi_zS)_{15}\}_{1+x}NbS_2$

hkl	$2\theta_{obs}$	$2\theta_{calc}$
0 1 0	15.50	15.26
4 0 0		15.29
1 1 1	17.52	17.01
2 1 0		17.08
$\bar{2}$ 1 1	18.38	18.06
2 1 1		18.33
0 0 3		18.72
$\bar{1}$ 0 3	19.25	18.91
1 0 3		19.31
0 1 3	24.42	24.24
$\bar{4}$ 1 2		24.65
4 0 3	24.86	24.87
0 0 4		25.04
4 1 2	25.73	25.48
1 0 4		25.55
0 0 5		31.45
0 2 1	31.78	31.46
8 0 1		31.83
7 1 1		32.02
$\bar{4}$ 1 4	32.50	32.71
0 2 2	33.36	33.34
4 1 4	33.65	33.97
0 1 5	35.38	35.13
$\bar{2}$ 1 5		35.63
0 2 3	36.24	36.29
2 1 5		36.37
$\bar{4}$ 1 6	43.86	43.38
0 0 7		44.60
0 2 5	44.59	44.60
4 1 6		44.87
12 0 1	47.76	47.84
$\bar{8}$ 2 4	50.35	50.55
0 0 8	51.36	51.40
$\bar{4}$ 2 6		51.60
4 2 6	52.94	52.92
0 0 9	58.70	58.40
1 0 9		58.77
16 0 0	64.32	64.18
0 4 0		64.18
00 11	72.87	73.09

$a = 23.2, b = 5.80, c = 14.23$ Å, $\beta = 93$.

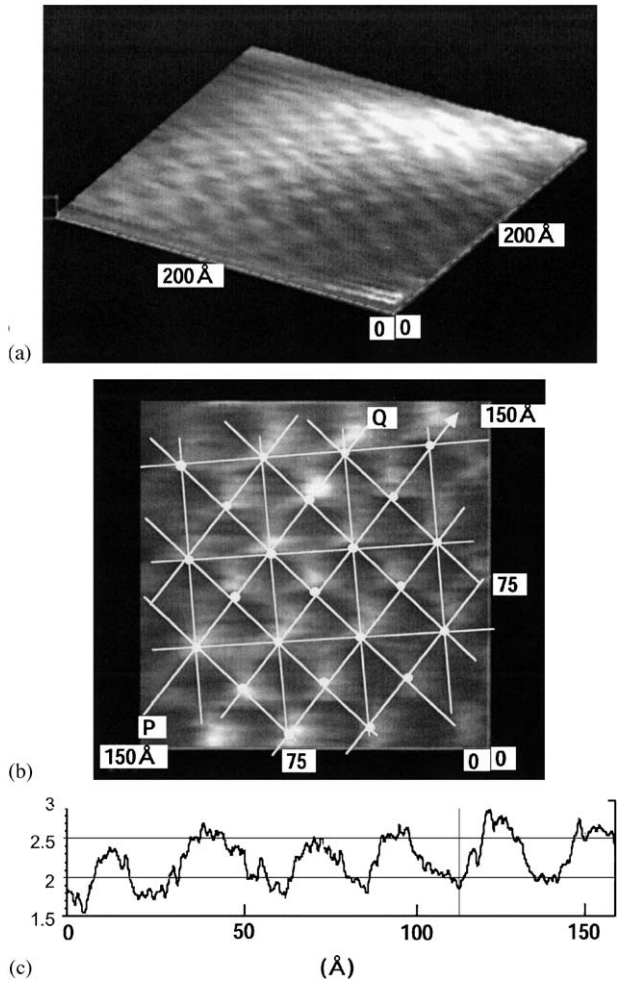

Fig. 9. (a) STM image of the NT of $\{(Nb_{1-z}Bi_zS)_{1.5}\}_{1+x}NbS_2$. (b) TOP view. Bright spots are arranged on a centered-rectangular mesh. (c) Height profile along the PQ line parallel to a tube axis. The nearest distance of the bright spots is about 28 Å. The STM image is explained in terms of the Moiŕe pattern which induced by rotational misorientation of the top layer relative to the underlying layer.

a period of about 23 Å in a circumferential direction. In fact, $2\theta_{obs}$ values are compatible with calculation values obtained with the common lattice parameters of $a = 23.2, b = 5.80$ and $c = 14.23$ Å. A STM image in Fig. 9 reveals the rows of bright large spots running along a tube axis and a near circumferential direction although no atomically resolved images are observed. They are arranged in centered-rectangular geometry and the nearest-neighbor distance is about 28 Å. Experimental errors encountered in measuring distances are within $\pm 5\%$, which are much smaller than a difference between the nearest-neighbor distance and the commensurate distance. Here it is remembered that a Moiŕe pattern is induced by rotational misorientation of the top layer relative to the underlying layer. In fact, such a STM image is often observed for graphite [23–25]. Therefore we may ascribe large spots in Fig. 9 to the rotation-induced Moiŕe pattern. The period of the Moiŕe pattern caused by a relative rotation φ is given by $D = d/(2\sin(\varphi/2)) \approx d/\varphi$, where d is the period of normal spots. In the present case d is about 4.1 Å, the nearest-neighbor distance of S atoms or metal atoms within a Q layer. If rotational misorientation of about 8° happens for the top layer and the underlying layer in forming a tubular crystal, a STM image in Fig. 9 would be observed. Lower magnified STM images reveal bright and dark streaks running along a tube axis. They are related to a faceted wall as discussed above. Here it is worth noting that the lattice parameters of $\{(Nb_{1-y-z}Pb_yBi_zS)_{1.5}\}_{1+x}NbS_2$ are comparable to those of $(Pb_2FeS_3)_{0.58}NbS_2$ [26] and $\{Pb(Mn,Nb)_{0.5}S_{1.5}\}_{1.15}NbS_2$ [27] in spite of the difference of atomic species in a Q layer. The latter two compounds belong to the 1.5Q/1H type of misfit-layer compounds and a Q layer consists of a three-atoms-thick layer, a central layer being constructed of a FeS or a (Mn,Nb)S layer sandwiched by two PbS layers. $(Nb_{1-y}La_yS)NbS_2$ in the last column in Table 3 is a unique misfit-layer compound discovered by Roesky et al. [28]. The crystals have a needle-shape. A $Nb_{1-y}La_yS$ layer is rotated by 45° in the (a, b) plane with respect to a NbS_2 layer and both the layers are commensurate in all directions. At present, however, it is not clear whether they are a tubular crystal or not. Fig. 10 shows the energy-dispersive X-ray spectroscopy (EDXS) spectra of the NT of $\{(Nb_{1-z}Bi_zS)_{1.5}\}_{1+x}NbS_2$, the lamellar crystal of $(BiS)_{1.08}NbS_2$ and the edge portion in Fig. 6(a). Because of surface contamination and the presence of amorphous layers on a wall an O K-line (not shown in Fig. 10) is more prominent for the NT and then the relative intensity of a Nb L to a S K-line is somewhat larger than that expected from the chemical composition by replacing a part of sulfur atoms by oxygen near a surface. However, no accurate determination of chemical compositions has been made because of a large overlap of Nb Lα (Energy of 2.17 keV), S $K\alpha$ (2.3 keV), Pb $M\alpha$ (2.35 keV) and Bi $M\alpha$ (2.42 keV) lines. In comparison with the lamellar crystal, it is found that a Bi concentration is very low for NTs as well as ribbon-like crystals, in consistency with the XRD result.

The temperature-dependent electrical resistance was measured for some MTs of $\{(Nb_{1-y}\ Pb_yS)_{1.5}\}_{1+x}NbS_2$. The results are shown in Fig. 11. It is found that resistance versus temperature curves fall into two distinct types with positive and negative slopes. For sample A the resistance increases with temperature. Its dependence become smaller at lower temperature and a whole appearance resembles that of a metallic carbon NT as shown in Fig. 12 in Ref. [29]. For samples B–D, on the other hand, it decreases with temperature monotonously. This behavior is very contrast with that of the lamellar crystals of most misfit-layer compounds containing a NbS_2 layer because they exhibit metallic

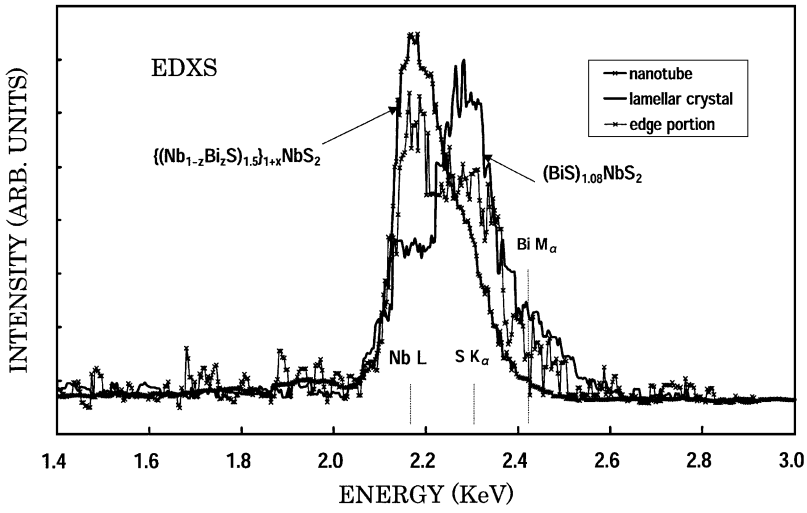

Fig. 10. EDXS spectra of the NT of $\{(Nb_{1-z}Bi_zS)_{1.5}\}_{1+x}NbS_2$, the lamellar crystal of $(BiS)_{1.08}NbS_2$ and the edge portion shown in Fig. 6.

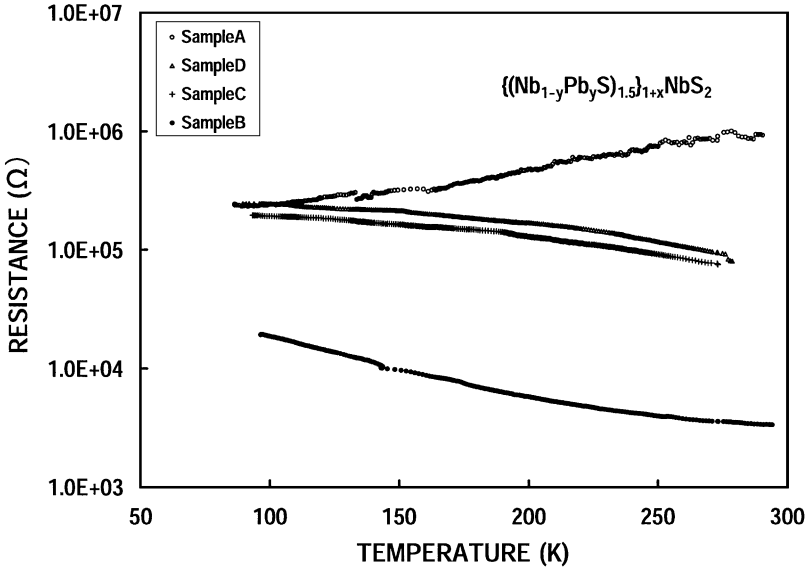

Fig. 11. Temperature dependent resistances of the filament-like crystals of $(Nb_{1-y}\ Pb_yS)_{1+x}NbS_2$.

properties, possessing incompletely filled Nb d_{z^2} states near the Fermi level. However, both metallic and semiconducting MTs have a resistance of the order of tens to hundreds kilo-ohm. Here it is worth noting that even weak Coulomb interaction causes strong perturbations in one-dimensional systems. The resulting system, known as a Luttinger liquid, is distinctly different from its two- and three-dimensional counterparts. Kane et al. [30] have theoretically predicted that an isolated electrical conductive nanotube should behave as a Luttinger liquid and the conductance reveals an anomalous power-law temperature dependence at high temperatures, that is, $G(T) \propto aT^{1-2g} + bT^{1-g/2}$, where g $(0<g<1)$ is the Luttinger parameter, which equals one in a Fermi liquid. The Luttinger-liquid behavior has experimentally been found for carbon NT bundles [31]. Then it is not surprising that our crystals behave as Luttinger liquid as well. Fig. 12 shows $\log(G)$ versus $\log(T)$ curves for samples A and C. It is found that they are constructed of two or three linear segments. For the semiconducting sample the conductance varies as $G(T) \propto T^{0.19}$ at temperatures below 120 K and $G(T) \propto T^{0.48}$ in the temperature range of 120–190 K. For the metallic sample it varies as $G(T) \propto T^{-0.75}$ in the range of 110–160 K. However, exponents at higher temperatures do not satisfy the theoretical prediction. We are planning four-probe measurements to avoid contact resistance effects.

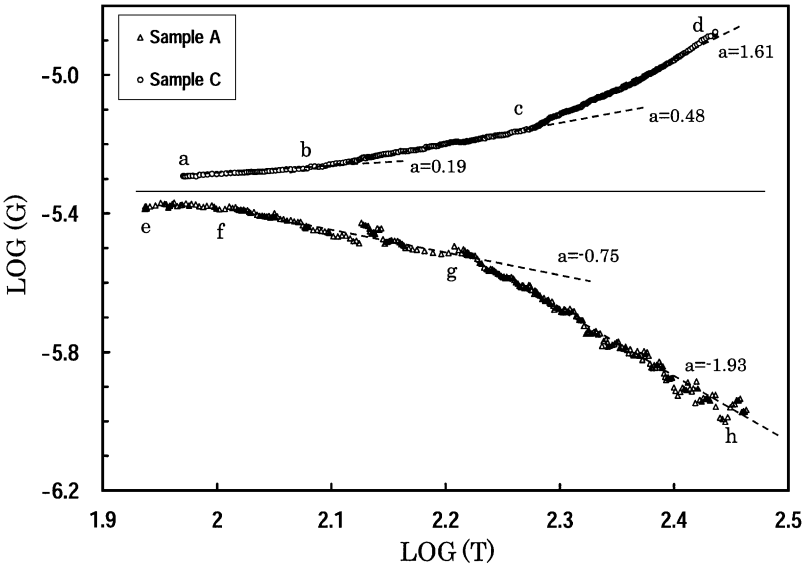

Fig. 12. LogG versus log T curves for samples A and C.

3.3. Lamellar crystals in the (Pb, Bi, Nb, S) system

Lamellar crystals in the (Pb, Bi, Nb, S) system, which are grown in the same silica tubes as filament-like crystals of $\{(Nb_{1-y-z}Pb_yBi_zS)_{1.5}\}_{1+x}NbS_2$, are identified as $(Pb_{1-y'}Bi_{y'}S)_{1+x'}(NbS_2)_n$ ($y = 0$, 0.33 and 1; $n = 1$ and 2). The $1+x'$ value is estimated from the incommesurability parameter α, using the relation $1 + x' = 2\alpha$. The XRD patterns in the reflection mode are shown in Fig. 13. They reveal strong (00ℓ) diffraction lines. The y' value is determined from the thickness of a Q layer. As a Bi content increases, the c lattice parameter decreases monotonously (see Table 3). Here it is remembered that intercalation of a Q layer has a minor influence on a H layer in misfit-layer compounds, so that we may assume that the thickness of a NbS_2 layer remains unchanged from that of 2H–NbS_2. In fact the c lattice parameter of $(PbS)_{1.13}(NbS_2)_2$ is nearly equal to the sum of the thickness of a PbS layer and two NbS_2 layers, i.e., $5.98 + 5.94 \times 2 = 17.86$ Å. Then a Q layer thickness (d_Q) is estimated from the c lattice parameters minus 5.94 Å to be 5.98, 5.82 and 5.50 Å for $(PbS)_{1.14}NbS_2$, $(Pb_{2/3}Bi_{1/3}S)_{1.14}NbS_2$ and $(BiS)_{1.08}NbS_2$, respectively. They are plotted approximately on the straight line $d_Q = 5.98 - 0.58y$. This is due to the fact that Pb substitution with Bi brings about a contracted Q layer in the c direction due to a reduced ion radius.

Fig. 14 shows the XRD patterns of $(BiS)_{1.08}NbS_2$, $(Pb_{2/3}Bi_{1/3}S)_{1.14}NbS_2$ and $(PbS)_{1.14}NbS_2$ in the transmission mode. Intensive lines are found at $\varphi = n\pi$ and $\varphi = (2n+1)\pi/2$ (n is integer). The former is derived from the parallel (200) planes of the Q layers while the latter is derived from both the parallel (020) planes of the Q layers and the $(0\,\mathbf{1}\,\bar{\mathbf{1}}\,0)$ planes of the H layers. Weak diffraction lines at $\varphi = (6n \pm 1)\pi/6$ may be attributed to the $(1\,0\,\bar{\mathbf{1}}\,0)$ and $(\mathbf{1}\bar{\mathbf{1}}00)$ planes of the H layers. As

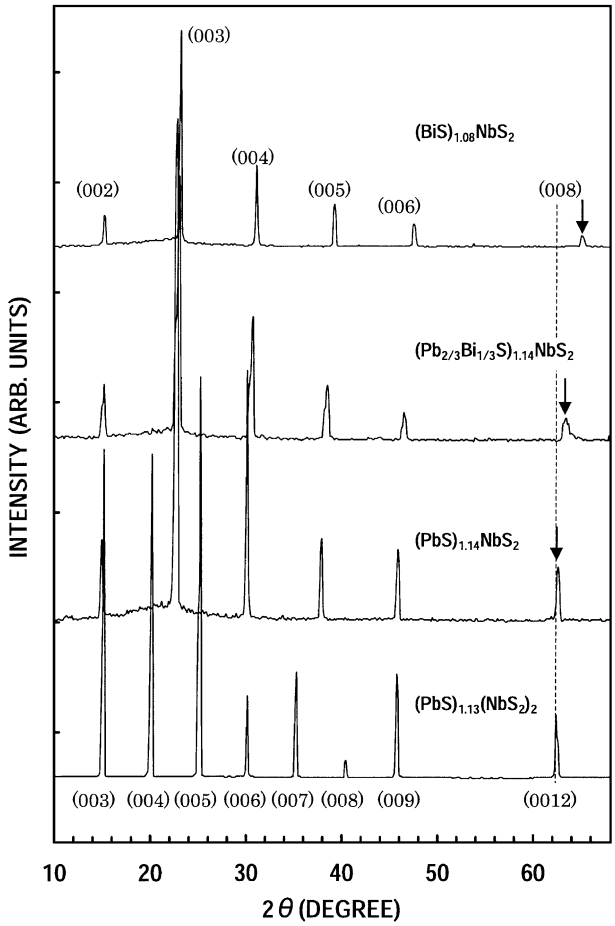

Fig. 13. XRD patterns of the lamellar crystals of $(BiS)_{1.08}NbS_2$, $(Pb_{2/3}Bi_{1/3}S)_{1.14}NbS_2$, $(PbS)_{1.14}NbS_2$ and $(PbS)_{1.14}(NbS_2)_2$ measured in the reflection mode.

$d_{(200)-Q}$, $d_{(020)-Q}$ and $d_{(01\bar{1}0)-H}$ are the spacings of the parallel (200) and (020) planes of the Q layers and the parallel $(0\mathbf{1}\bar{\mathbf{1}}0)$ planes of the H layers, respectively, the

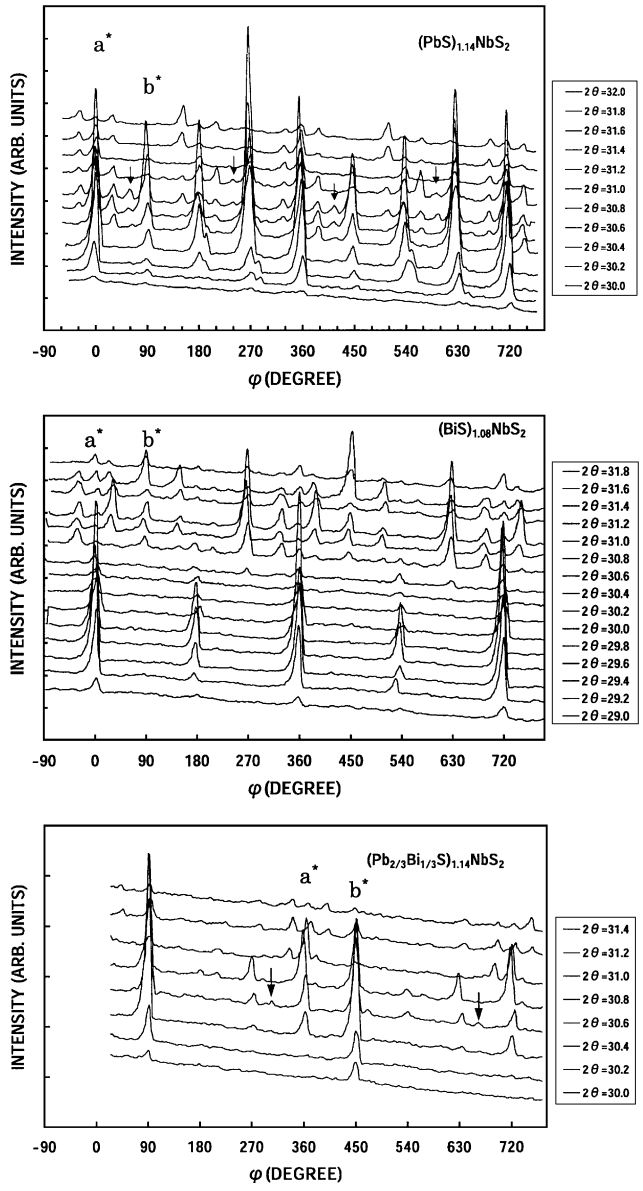

Fig. 14. XRD patterns of the lamellar crystals of $(PbS)_{1.14}NbS_2$, $(BiS)_{1.08}NbS_2$ and $(Pb_{2/3}Bi_{1/3}S)_{1.14}NbS_2$ measured in the transmission mode. Diffraction peaks marked by an arrow indicate the existence of stacking faults which induces the 30° or 90° rotation of the H layers against the Q layers.

relationships $d_{(200)-Q} = d_{(020)-Q} = d_{(01\bar{1}0)-H}$ hold for ideal tetragonal and hexagonal lattices because $a_Q = b = \sqrt{3}a_H$. A slight deviation from the ideal structure causes a difference in 2θ values. If $a_Q > b$, then $2\theta_{(200)-Q} < 2\theta_{(020)-Q}$. The a and b lattice parameters obtained are summarized in Table 4. The lattice parameters for $(BiS)_{1.08}NbS_2$ are almost in agreement with those of $(BiS)_{1.10}NbS_2$ which have been determined by Gotoh et al. [32]. As a Bi content increases, lattice parameters in the (a,b) plane are changed more complicatedly than the c lattice parameter. Particularly, the b/a_Q ratio is reversed between the pure compounds and the mixed compound. Gotoh et al. have indicated that Bi–Bi bonds and non-bonded S–S pairs are formed along a mutually incommensurate direction. Then apparently complex variations in the (a,b) plane may be due to the rearrangement of metal species or atomic disorder in the mixed compound. Finally, it should be noted in Fig. 14 that there are stacking faults in a crystal. Taking the six-fold symmetry of a NbS_2 layer into account, a H layer rotates by 30° or 90° with respect to the underlying Q layer. Such orientation variants have been studied in detail by Kuypers et al. [33]. Then if a H layer rotates by 30° or a Q layer rotates by 90°, a commensurate direction turns to coincide with the a direction of a crystal with no stacking faults. This is a reason why filament- and ribbon-like crystals often grow in a direction rotated by 30°.

4. Conclusions

Our attempts to prepare the NTs or MTs of $(PbS)_{1.14}(NbS_2)_2$, $(BiS)_{1.08}(NbS_2)_2$, $(Pb_{2/3}Bi_{1/3}S)_{1.14}(NbS_2)_2$, $(Pb_{0.82}Bi_{0.18}S)_{1.14}(NbS_2)_2$ and $(SmS)_{1.19}(TaS_2)_2$ by chemical vapor transport reaction are partially successful. The NTs and MTs of $(SmS)_{1.19}TaS_2$ were obtained, which were grown together with TaS_2 NTs or MTs in a mixture form or as a composite crystal. Although the thick walled multilayer cylindrical tubes of diameter extending 100 μm were also found for $(BiS)_{1.08}NbS_2$ as well as $(SmS)_{1.19}TaS_2$, few NTs or MTs of diameters of the order of 1 μm were obtained for $(Pb_{1-y'}Bi_{y'}S)_{1+x'}(NbS_2)_n$ ($n = 1$ and 2). Instead of them $\{(Nb_{1-y-z}\ Pb_yBi_zS)_{1.5}\}_{1+x}NbS_2$ NTs and MTs were synthesized abundantly. Some filament- and ribbon-like crystals are grown from the edge of a lamellar crystal. An elongating direction or a tube axis is parallel to the commensurate b direction. Their compounds belong to the 1.5Q/1H type of misfit-layer compounds and the incommensurability parameters are very close to the rational ratio 4/7. Thin-walled NTs have a corrugated wall consisting of many strips running along a tube axis. The orthorhombic lattice of $\{(Nb_{1-y}Pb_yS)_{1.5}\}_{1+x}NbS_2$ is changed to the monoclinic one by substituting Pb with Bi, although their lattice parameters except for β are scarcely dependent on it. This is due to the low concentrations of the metal species. Lamellar crystals grown at the same time are identified to be $(PbS)_{1.14}NbS_2$, $(PbS)_{1.13}(NbS_2)_2$, $(BiS)_{1.10}NbS_2$, $(Pb_{2/3}Bi_{1/3}S)_{1.14}NbS_2$ and $(Pb_{0.82}Bi_{0.18}S)_{1.14}NbS_2$. The c lattice parameter decreases linearly with a Bi content. This fact suggests that Bi is in a higher valence state than Pb. Preliminary temperature-dependent electrical resistance measurements have been made for the filament-like crystals of $\{(Nb_{1-y}Pb_yS)_{1+x}\}_{1.5}NbS_2$. Two distinct types of characteristic curves with positive and negative temperature coefficients are obtained.

Table 4
Lattice parameters and the incommensurability parameters of misfit-layer compounds of our interest

Material	Polytype	Lattice parameters					α	Crystals[b]	Ref.
		a_Q	a_H	b	c	β			
$(PbS)_{1.14}NbS_2$	1Q/1H	5.82	3.33	5.79	11.92		0.572	L	This work
$(PbS)_{1.13}(NbS_2)_2$	1Q/2H	5.84	3.31	5.79	17.85		0.567	L	This work
$(Pb_{2/3}Bi_{1/3}S)_{1.14}NbS_2$	1Q/1H	5.80	3.31	5.84	11.76		0.571	L	This work
$(BiS)_{108}NbS_2$	1Q/1H	6.03	3.27	5.73	11.43		0.542	L	This work
$\{(Nb_{1-y-z}Pb_yBi_zS)_{1.5}\}_{1+x}NbS_2$	1.5Q/1H	23.2	3.35[a]	5.80	14.23	90–93	0.577	F	This work
$(Pb_2FeS_3)_{0.58}NbS_2$	1.5Q/1H	5.763	3.33	5.798	14.081		0.578	L	[26]
$\{Pb(Mn,Nb)_{0.5}S_{1.5}\}_{1.15}NbS_2$	1.5Q/1H	5.790	3.33	5.788	14.326		0.575	L	[27]
$(Nb_{1-y}La_yS)NbS_2$	1Q/1H	9.995		5.827	23.817			F	[28]

[a]This value is obtained, using the relation $a_H = b/\sqrt{3}$.
[b]The notations L and F denote lamellar and filament-like crystals, respectively.

Acknowledgments

The author wishes to thank Mr. N. Takezawa and Mr. K. Kikuchi for their co-operation in SEM observations.

References

[1] S. Iijima, Nature 354 (1991) 56.
[2] M.S. Dresselhaus, G. Dresselhaus, Ph. Arouris (Eds.), Carbon Nanotubes, Synthesis, Structure, Properties and Applications, Springer, Tokyo, 2001.
[3] R. Tenne, L. Margulis, M. Genut, G. Hodes, Nature 360 (1992) 444.
[4] J. Chen, S.L. Li, Z.L. Tao, F. Gao, Chem. Commun. 8 (2003) 980.
[5] J. Chen, Z. Tao, S.L. Li, X.B. Fan, S.L. Chou, Adv. Mater. 15 (2003) 1379.
[6] Pure Appl. Chem. 74 (2002) 1545;
M. Nath, C.N.R. Rao, Angew. Chem. Int. Ed. 41 (2002) 3451.
[7] M. Remškar, A. Mrzel, A. Jesih, F. Lévy, Adv. Mater. 14 (2002) 680.
[8] M. Nath, S. Kar, A.K. Raychaudhuri, C.N.R. Rao, Chem. Phys. Lett. 368 (2003) 690.
[9] M. Nath, C.N.R. Rao, J. Am. Chem. Soc. 123 (2001) 4841.
[10] M. Hershfinkel, L.A. Gheber, V. Volterra, J.L. Hutchison, L. Margulis, R. Tenne, J. Am. Chem. Soc. 116 (1994) 1914.
[11] M. Remškar, Z. Škraba, F. Cléton, R. Sanjineés, F. Lévy, Surf. Rev. Lett. 5 (1998) 423.
[12] Surf. Sci. 433–435 (1999) 637;
M. Remškar, A. Mrzel, Vacuum 71 (2003) 177.
[13] A. Rothschild, J. Sloan, R. Tenne, J. Am. Chem. Soc. 122 (2000) 5165.
[14] M. Nath, C.N.R. Rao, Chem. Commun. 21 (2001) 2236.
[15] J. Chen, S.L. Li, Z.L. Tao, J. Alloys and Compds. 356–357 (2003) 413.
[16] R. Dominko, M. Gaberscek, D. Arcon, A. Mrzel, M. Remškar, D. Mihailovic, S. Pejovnik, J. Jamnik, Electrochim. Acta 48 (2003) 3079.
[17] L. Guemas, P. Rabu, A. Meerschaut, J. Rouxel, Mater. Res. Bull. 23 (1988) 1061.
[18] D. Bernaerts, S. Amelinckx, G. Van Tendelloo, J. Van Landuyt, J. Cryst. Growth 172 (1997) 433.
[19] A. Gómez-Herrero, A.R. Landa-Cánovas, S. Hansen, L.C. Otero-Díaz, Micron 31 (2000) 587.
[20] M. Remškar, Z. Škraba, M. Regula, Adv. Mater. 10 (1998) 246.
[21] G.A. Wiegers, A. Meetsma, R.J. Haange, J.L. de Boer, J. Less Common Met. 168 (1991) 347.
[22] M. Remskar, Z. Skraba, F. Cléton, R. Sanjinés, F. Lévy, Appl. Phys. Lett. 69 (1996) 351.
[23] M. Kuwabara, D.R. Clarke, D.A. Smith, Appl. Phys. Lett. 56 (1990) 2396.
[24] J. Xhie, K. Sattler, M. Ge, N. Venkateswaren, Phys. Rev. B 47 (1993) 15835.
[25] Z.Y. Rong, Phys. Rev. B 50 (1994) 1839.
[26] J. Solid State Chem. 142 (1999) 461;
Y. Moëlo, A. Lafond, C. Deudon, N. Coulon, M. Lancin, A. Meerschaut, C. R. Acad. Sci. Paris 325 (1997) 287.
[27] C. Deudon, A. Lafond, O. Leynaud, Y. Moëlo, A. Meerschaut, J. Solid State Chem. 155 (2000) 1.
[28] R. Roesky, A. Meerschaut, A. van der Lee, J. Rouxel, Mater. Res. Bull. 29 (1994) 1149.
[29] H. Dai, in: M.S. Dresselhaus, G. Dresselhaus, Ph. Arouris (Eds.), Carbon Nanotubes, Synthesis, Structure, Properties and Applications, Springer, Tokyo, 2001, p. 47.
[30] C. Kane, L. Balents, M.P.A. Fisher, Phys. Rev. Lett. 79 (1997) 5086.
[31] M. Bockrath, D.H. Cobden, J. Lu, A.G. Rinzler, R.E. Smalley, L. Balents, P.L. McEuen, Nature 397 (1999) 598.
[32] Y. Gotoh, J. Akimoto, M. Goto, Y. Oosawa, M. Onoda, J. Solid State Chem. 116 (1995) 61.
[33] S. Kuypers, J. van Landuyt, S. Amelinckx, J Solid State Chem. 86 (1990) 212.